Chemical Engineering Journal 459 (2023) 141662

Contents lists available at ScienceDirect

Chemical Engineering Journal

journal homepage: www.elsevier.com/locate/cej

Interfacial synthesis of strongly-coupled δ-MnO_2/MXene heteronanosheets for stable zinc ion batteries with Zn^{2+}-exclusive storage mechanism

Lisha Wu [a,b,1], Yingying Mei [a,1], Yuanhao Liu [a], Wen Xu [a], Minghui Zhang [a], Yanfeng Dong [a,*], Zhong-Shuai Wu [b,c,*]

[a] Department of Chemistry, College of Sciences, Northeastern University, Shenyang 110819, China
[b] State Key Laboratory of Catalysis, Dalian Institute of Chemical Physics, Chinese Academy of Sciences, Dalian 116023, China
[c] Dalian National Laboratory for Clean Energy, Chinese Academy of Sciences, Dalian 116023, China

ARTICLE INFO

Keywords:
Zinc ion batteries
Manganese dioxide
MXene
Long cycling life

ABSTRACT

Low-cost and nontoxic manganese dioxide (MnO_2) cathodes have shown promising application in high-capacity and high-voltage rechargeable zinc ion batteries (ZIBs), but suffer from limited cycling life and energy density mainly due to poor electrical conductivity and structural failure induced by manganese dissolution and H^+/Zn^{2+} co-intercalation in traditional aqueous electrolytes. Herein, two-dimensional strongly-coupled δ-MnO_2/MXene heteronanosheets are efficiently developed for high-performance ZIBs, which mainly includes an in-situ polymerization of dopamine on Ti_3C_2 MXene surface and subsequent redox reaction between $KMnO_4$ and polydopamine. Benefited from the conductive MXene nanosheets for fast electron transfer, and the thin thickness of δ-MnO_2 nanosheets for improved Zn^{2+} insertion kinetics and structural stability, the δ-MnO_2/MXene heteronanosheets exhibit unique Zn^{2+}-exclusive storage mechanism without proton storage induced disadvantages (e.g., Mn dissolution in traditional aqueous electrolytes) and superior zinc storage performance in 0.5 M zinc triflate in triethyl phosphate organic electrolyte ($Zn(OTf)_2$/TEP), offering a capacity of ~163 mAh g^{-1} at 100 mA g^{-1}, a high capacity retention of 84.5 % after 1000 cycles, and an areal capacity of 1.9 mAh cm^{-2} when the mass loading is up to 10.5 mg cm^{-2}. This work provides unique Zn^{2+}-exclusive storage mechanism of δ-MnO_2 in organic electrolyte and opens up a new approach for building high-performance ZIBs.

1. Introduction

Rechargeable zinc ion batteries (ZIBs) hold great potentials in renewable energy fields as an alternative to prevailing lithium-ion batteries mainly benefited from several merits of Zn metal, such as low cost, high theoretical capacity (820 mAh g^{-1} or 5855 mAh cm^{-3}), and suitable anode potential (-0.76 V vs. standard hydrogen electrode) [1–4]. As a key component in ZIBs, advanced cathode plays significant role in determining the electrochemical performance of ZIBs. Especially, low-cost and abundant manganese dioxide (MnO_2) has been deemed as one of the most promising candidates for ZIBs due to its high theoretical capacity (308 mAh g^{-1}) and high voltage plateau [5,6]. However, the undesirable conductivity (10^{-5}-10^{-6} S cm^{-1}) [7] and manganese dissolution issues in traditional aqueous electrolytes (e.g., 1 M $ZnSO_4$) [8,9] usually result in low capacity and limited cycling life, seriously hindering the practical application of MnO_2 cathodes for ZIBs [10,11].

To address the mentioned challenges, one efficient strategy is to rationally design and construct advanced MnO_2 cathodes, such as interlayer engineering [12], defective engineering [13], and MnO_2 based hybrid cathodes [14], among which, the latter strategy is considered to be most effective due to the rich choices of various functional materials and different designs of hybrid nanostructures [15,16]. Notably, as a new star of 2D materials after graphene, transition metal carbides and nitrides (MXene) nanosheets possess high conductivity up to 20,000 S cm^{-1} and abundant functional groups (e.g., –OH, and –F), providing possibility to construct advanced MnO_2/MXene hybrid cathodes for high-performance ZIBs [17–19], in which MXene nanosheets can effectively improve the conductivity and structural integrity of MnO_2. For example, the gas-phase spray drying strategy was employed to encapsulate MnO_2 nanoparticles and MXene nanosheets [20], hence the assembled MXene-MnO_2 hybrid cathode displayed superior zinc storage performance (e.g., a capacity retention of 90.6 % at 100 mA g^{-1}

* Corresponding authors at: Department of Chemistry, College of Sciences, Northeastern University, Shenyang 110819, China.
E-mail addresses: dongyanfeng@mail.neu.edu.cn (Y. Dong), wuzs@dicp.ac.cn (Z.-S. Wu).
[1] These authors contributed equally to this work.

https://doi.org/10.1016/j.cej.2023.141662

Available online 1 February 2023

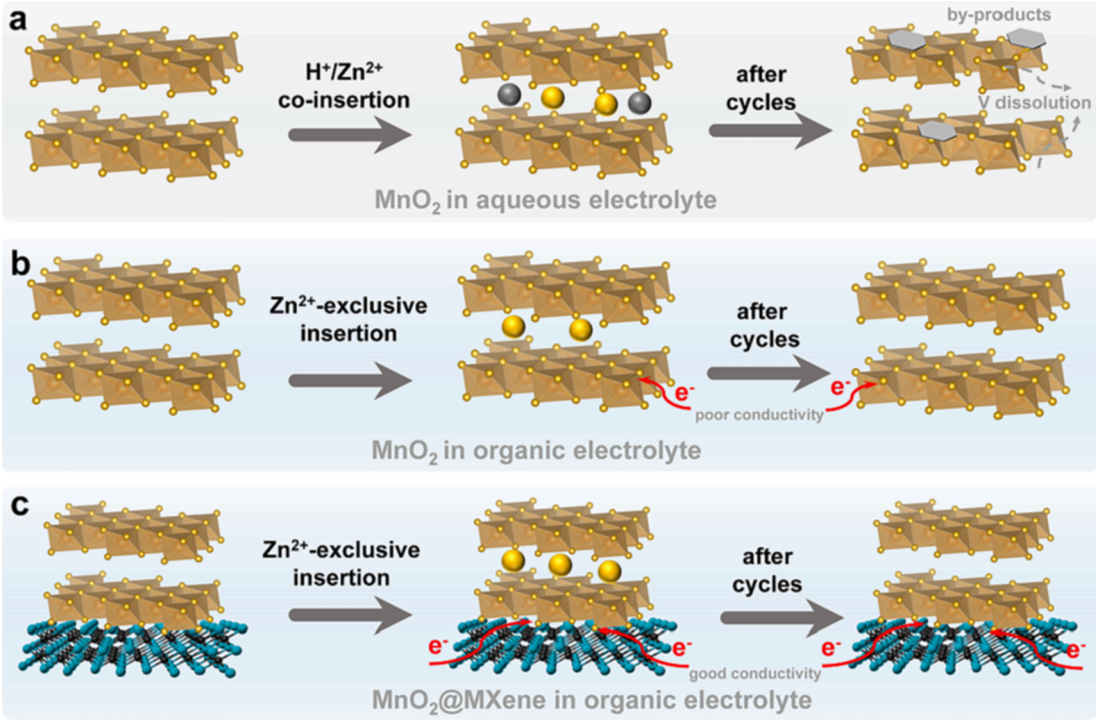

Fig. 1. Schematic illustration of the superiority of MnO_2@MXene in organic electrolyte. (a) MnO_2@MXene cathodes in aqueous electrolyte suffer from structural collapse and the formation of by-products. (b) Organic electrolyte ensures structural stability of MnO_2@MXene cathodes. (c) Ti_3C_2 MXene nanosheets with good conductivity enable fast electron transfer kinetics.

after 2000 cycles) to pure MnO_2 (a capacity retention of 21.4 %). Moreover, V_2CT_x MXene was introduced for the uniform MnO_2 nanosheets via in-situ growth strategy, and a high specific capacity of 119.2 mAh g^{-1} at 10 A g^{-1} was achieved in the resulting manganese-vanadium hybrid cathode after 10,000 cycles [21]. Another efficient strategy is to rationally design suitable electrolytes. For instance, introducing additives (e.g., Mn^{2+} ions) into aqueous electrolytes (e.g., $ZnSO_4$) is able to change the dissolution equilibrium of Mn^{2+} ions from MnO_2 and thus greatly suppress Mn dissolution [22]. Moreover, rationally regulating the concentration of Mn^{2+} ions to 0.005 mol L^{-1} can achieve both MnO_2/Mn^{3+} and MnO_2/Mn^{2+} redox conversion in a stable and reversible manner within the broad voltage window of ~2.3 V [23]. Despite great progress, rational design and efficient synthesis of 2D well-defined MnO_2/MXene hybrids are still rarely reported since MnO_2 with desired crystal structures and nanostructures are usually uncontrollably deposited on MXene nanosheets. Meanwhile, H^+/Zn^{2+} co-insertion into MnO_2 matrix usually results in pH variation of aqueous electrolytes and the irreversible formation of by-products (e.g., zinc sulfate hydroxide) [24], and correspondingly, inferior cycling life is frequently recorded. Therefore, it is of great importance yet challenging to develop a controllable synthesis strategy for MnO_2/MXene hybrids and explore novel zinc storage mechanisms in new electrolytes for stable ZIBs.

Considering that layered δ-MnO_2 greatly facilitates reversible Zn^{2+} ion intercalation, herein 2D δ-MnO_2@MXene heteronanosheets are synthesized via in-situ polymerization of dopamine (DA) on MXene nanosheets and subsequent vertical deposition of δ-MnO_2 nanoflakes on MXene based on the redox reaction between polydopamine (PDA) and $KMnO_4$. The strongly-coupled MnO_2@MXene heteronanosheets present thin thickness of ~15 nm, and can be assembled into free-standing films via filtration with graphene or phase inversion-freeze drying processes. Importantly, the resulting MnO_2@MXene film cathodes in organic electrolyte of 0.5 M zinc triflate ($Zn(OTf)_2$) in intrinsic safe triethyl phosphate (TEP) solvent show fast reaction kinetics and stable structural stability due to the contribution of MXene nanosheets and organic electrolytes, avoiding the formation of by-products, Mn dissolution, and structural collapse in aqueous electrolyte and sluggish reaction kinetics in pure MnO_x cathode (Fig. 1). Therefore, the as-assembled Zn//MnO_2 batteries exhibit stable charge/discharge processes for up to 1000 cycles and a high capacity retention of 84.5 %. This work provides a reliable way to develop advanced organic Zn-MnO_2 batteries with unique Zn^{2+}-exclusive storage mechanism.

2. Experimental

2.1. Material synthesis

Interfacial synthesis of MnO_2@MXene heteronanosheets: MnO_2@MXene heteronanosheets were synthesized by in-situ self-polymerization of dopamine on Ti_3C_2 MXene nanosheets and subsequent reduction of $KMnO_4$ by PDA. Typically, 4 mL delaminated few-layer MXene nanosheets (5 mg mL^{-1}, 11 Technology Co., ltd.) were pipetted into 50 mL tris-buffer solution (10 mM, pH = 8.5), followed by stirring for 1 h. Subsequently, 50 mg dopamine hydrochloride was added into above solution and stirred for 9 h at room temperature, which was subjected to centrifugation and washing for five times to obtain PDA@MXene nanosheets. Then, the resulting samples were dispersed in 70 mL $KMnO_4$ solution (5 mM) under stirring for 4 h, and the final products of MnO_2@MXene heteronanosheets were collected by centrifugation and washing, and freeze-drying. Moreover, MnO_2@MXene heteronanosheets with different ratio of MXene to MnO_2 were fabricated and compared by varying the dose of Ti_3C_2 MXene suspension. In addition, MnO_2 nanospheres were synthesized according to the above method except for the absence of MXene nanosheets.

Synthesis of MnO_2@MXene based film electrodes: MnO_2@MXene based thin film electrodes were prepared with the help of electrochemical exfoliated graphene (EG) nanosheets (Fig. S1). Specially, EG nanosheets were firstly mixed with MnO_2@MXene suspension (5 mg mL^{-1}, 5.54 mL), then MnO_2@MXene based thin film was fabricated by filtering the mixed suspension via vacuum filtration and dried at 80 °C in vacuum. Afterwards, MnO_2@MXene based thick films were prepared via

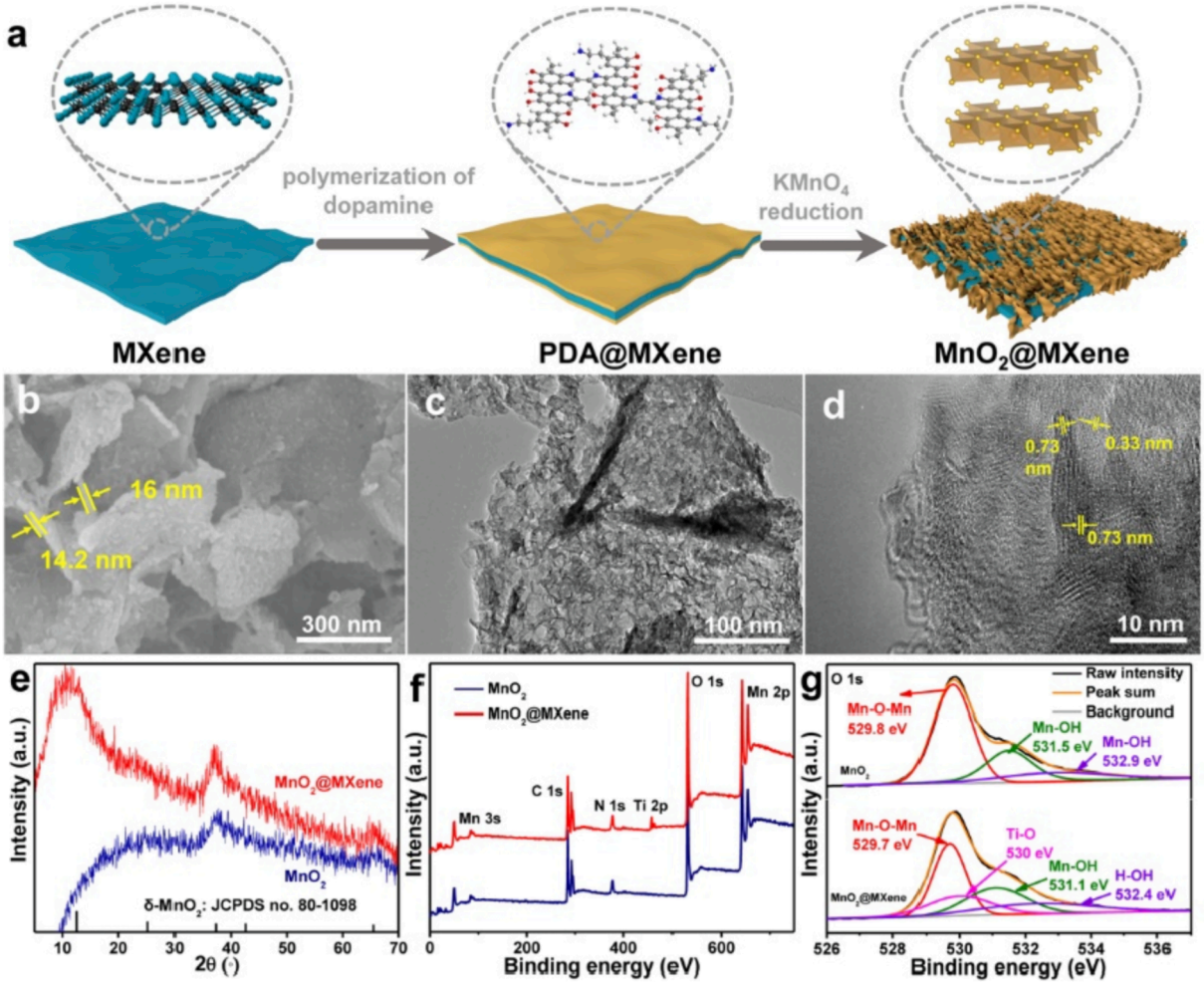

Fig. 2. (a) Schematic illustration of the preparation of MnO_2@MXene heteronanosheets. (b) SEM image, (c) TEM image, and (d) HRTEM image of MnO_2@MXene. (e) XRD pattern, (f) XPS spectra, and (g) high resolution O1s spectra of MnO_2@MXene.

a modified phase-inversion strategy [25–28], which facilitates the construction of free-standing porous film electrodes. Specially, a slurry consisting of MnO_2@MXene heteronanosheets, polyvinylidene difluoride (PVDF), and carbon black with a mass ratio of 7:2:1 dispersing in *N*-methyl-2-pyrrolidone solvents was injected into a home-made polyethylene terephthalate mold, which was subject to immersion in deionized water for 8 h and subsequent freeze-drying to obtain the free-standing thick electrodes. The as-synthesized thick films with a high mass loading of 10.5 mg cm^{-2} were cut into square-like shape with size of 0.5 × 0.5 cm for the assembly of ZIBs.

2.2. Material characterization

The morphology and chemical composition of MnO_2@MXene heteronanosheets were characterized by scanning electron microscopy (SEM, SU8010, HITACHI) coupled with an energy dispersive X-ray spectroscopy (EDS) detector, transmission electron microscope (TEM, JEM-2100) with elemental dispersive spectrometer, high resolution TEM (HRTEM, JEM-2100), X-ray diffraction patterns (XRD, PANalytical Empyrean), X-ray photoelectron spectroscopy (XPS, Thermo Scientific K-Alpha +), Raman spectroscopy (Xplora, HORIBA JOBIN YVON S.A. Company), and Fourier transform infrared spectroscopy (FTIR, TENSOR 27).

2.3. Electrochemical measurement

To measure the ion conductivity of electrolytes, glass fiber separator saturated with targeted electrolytes was sandwiched by two stainless steels, and thus the ionic conductivities of electrolytes can be calculated according to the equation of $\sigma = \frac{l}{R \times S}$, in which l (cm), R (Ω) and S (cm^2) represent the thickness of separator, bulk resistance in electrochemical impedance spectroscopy (EIS) test and electrode area, respectively. Then, after measurement of the ionic conductivities of targeted electrolytes at different temperatures ranging from 0 to 60 °C, activation energies (E_a) could be calculated based on Arrhenius equation of $\sigma = \frac{A}{T} * \exp(-E_a/RT)$.

Zn//Zn symmetrical batteries were assembled with Zn foils as electrodes, 0.5 M $Zn(OTf)_2$/TEP as electrolytes, and glass fiber membrane as separators. For Zn//MnO_2 batteries, MnO_2@MXene film, Zn foil, and glass fiber membrane were used as cathode, anode, and separator in coin-type cells (CR2016), respectively. Moreover, 0.5 M $Zn(OTf)_2$/TEP and 2 M $ZnSO_4$ with 0.2 M $MnSO_4$ additive were prepared as organic and aqueous electrolyte, respectively. Galvanostatic charge/discharge (GCD) profiles, rate capability, and cycling performance of ZIBs were conducted with LAND (CT2001A) test system. Cyclic voltammetry (CV) curves, linear sweep voltammetry (LSV) measurements, and EIS tests with the amplitude of 5 mV and the frequency from 100 kHz to 0.01 Hz were carried out with an electrochemical workstation (CHI 660E).

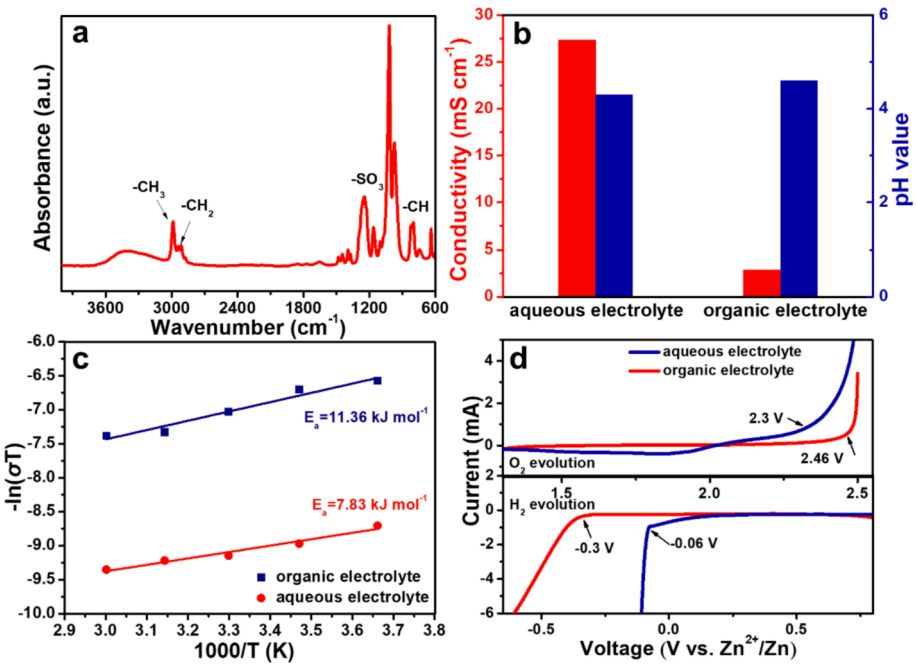

Fig. 3. (a) FTIR spectrum of organic electrolyte. (b) Ionic conductivity and pH value of aqueous and organic electrolytes. (c) Arrhenius plots of aqueous and organic electrolytes. (d) LSV curves of MnO_2@MXene in organic and aqueous electrolytes.

3. Results and discussion

The MnO_2@MXene heteronanosheets were fabricated through an in-situ self-polymerization of dopamine and subsequent MnO_2 deposition on Ti_3C_2 MXene nanosheets through the redox reaction between $KMnO_4$ and PDA, as illustrated in Fig. 2a. Specifically, dopamine was in-situ self-polymerized to form a PDA layer on few-layer Ti_3C_2 MXene nanosheets in tris-buffer solution (pH = 8.5) to obtain PDA@MXene hybrid nanosheets with smooth surface (Fig. S2). Subsequently, MnO_2 nanoflakes were grown on MXene nanosheets via the redox reaction between $KMnO_4$ and PDA, resulting in MnO_2@MXene heteronanosheets (Fig. 2a). As shown in Fig. 2b, the heteronanosheets display obvious 2D structures and rough surface due to the presence of thin and vertical MnO_2 nanosheets (Fig. 2b-c). HRTEM image further demonstrates clear diffraction fringes of MnO_2 with interlayer spacings of ~0.33 and 0.73 nm attributed to (0 0 2) and (0 0 1) planes of δ-MnO_2 (Fig. 2d), respectively. Elemental mapping analysis confirms the uniform and apparent distribution of Mn, O, Ti, and C on the selected area of MnO_2@MXene heteronanosheets (Fig. S3). For comparison, MnO_2 microspheres were fabricated via self-polymerization of dopamine into PDA microspheres with smooth surface and subsequent $KMnO_4$ reduction by PDA, resulting in MnO_2 microspheres decorated with nanosheets (Fig. S4).

Various characterizations were conducted to investigate the evolution of chemical composition during the preparation of MnO_2@MXene heteronanosheets. After PDA coating on MXene, most diffraction peaks of MXene in XRD patterns become weaker (Fig. S5a), and notably, the (0 0 2) peak of Ti_3C_2 MXene at 7.4° can't be observed in the range from 5° to 90° for PDA@MXene sample because the presence of PDA coating layers significantly enlarges the interlayer spacing of MXene nanosheets. Meanwhile, Raman spectrum further demonstrates the presence of Ti–O and Ti–C signals at 220 and 672 cm^{-1} (Fig. S5b), respectively. When MnO_2 nanoflakes are vertically decorated on MXene nanosheets, the typical but weak diffraction peaks at 12.0°, 25.3°, 37.3°, and 42.7° are observed (Fig. 2e), corresponding to (0 0 1), (0 0 2), (1 1 1), and (1 1 2) crystal plane of birnessite-type manganese oxide (JCPDS no. 80-1098), respectively, demonstrating the successful preparation of low-crystalline δ-MnO_2 on MXene. In addition, XPS analysis demonstrates the presence of Mn, O, Ti, and C elements (Fig. 2f), which is consistent with elemental mapping results in Fig. S3. Moreover, N element can be detected in the MnO_2@MXene heteronanosheets (Fig. 2f), possibly due to the presence of trace amount of N containing product from the redox reaction between $KMnO_4$ and PDA. In addition, four peaks at 529.7, 530.0, 531.1, and 532.4 eV were performed from the high-resolution O 1 s spectrum after peak deconvolution, which are assigned to the signals of Mn–O–Mn, Ti–O, Mn–OH, and H–OH (Fig. 2g), respectively [29,30].

To explore new zinc storage behavior (e.g., Zn^{2+}-exclusive storage mechanism) of MnO_2@MXene heteronanosheets for excellent electrochemical performance, an organic electrolyte ($Zn(OTf)_2$/TEP) comprised of 0.5 M $Zn(OTf)_2$ salt and TEP solvent was specially developed. Signals at 2912 cm^{-1} and 2986 cm^{-1} in the FTIR spectroscopy of the organic electrolyte are assigned to the $–CH_2$ and $–CH_3$ asymmetric stretching modes (Fig. 3a), respectively [31]. Meanwhile, peaks in the range of 975–1163 cm^{-1} further indicate the presence of phosphate [32,33]. The organic electrolyte exhibits higher pH value of 4.6 and lower ionic conductivity of 2.83 mS cm^{-1} than aqueous electrolyte (pH = 4.3, 27.31 mS cm^{-1}), mainly due to the high activity of water molecules (Fig. 3b). Therefore, higher E_a of 11.36 kJ mol^{-1} was calculated for $Zn(OTf)_2$/TEP electrolyte compared with 7.83 kJ mol^{-1} for aqueous electrolyte (Fig. 3c and S6) [34,35]. In addition, LSV measurements of organic electrolyte further demonstrate a broad voltage window of -2.5 to 2.5 V in Zn//MnO_2 batteries with organic electrolyte, which is wider than the counterpart with aqueous electrolyte (-0.3 to 2.46 V) (Fig. 3d). Furthermore, the organic electrolyte endows Zn foil anodes with high reversibility and dendrite-free features for long cycling life (1000 h) in Zn//Zn symmetrical batteries (Fig. S7).

The electrochemical performance of MnO_2@MXene based thin film electrode in the organic electrolyte of $Zn(OTf)_2$/TEP were systematically investigated. As shown in Fig. 4a, b, the MnO_2@MXene thin film cathode in the 2 M $ZnSO_4$ aqueous electrolyte displays two obvious pairs of redox peaks at 1.20/1.33 V and 1.62/1.67 V (Fig. 4a), which correspond to H^+ (region I) and Zn^{2+} intercalation (region II), respectively (Fig. 4b) [36], respectively. Interestingly, a cathodic peak at ~1.30 V and an anodic peak at ~1.56 V can be observed in the case of the organic electrolyte within the wide voltage window of 0.2–2.1 V (vs. Zn/Zn^{2+}), and there is no proton storage behavior (Region I) (Fig. 4a).

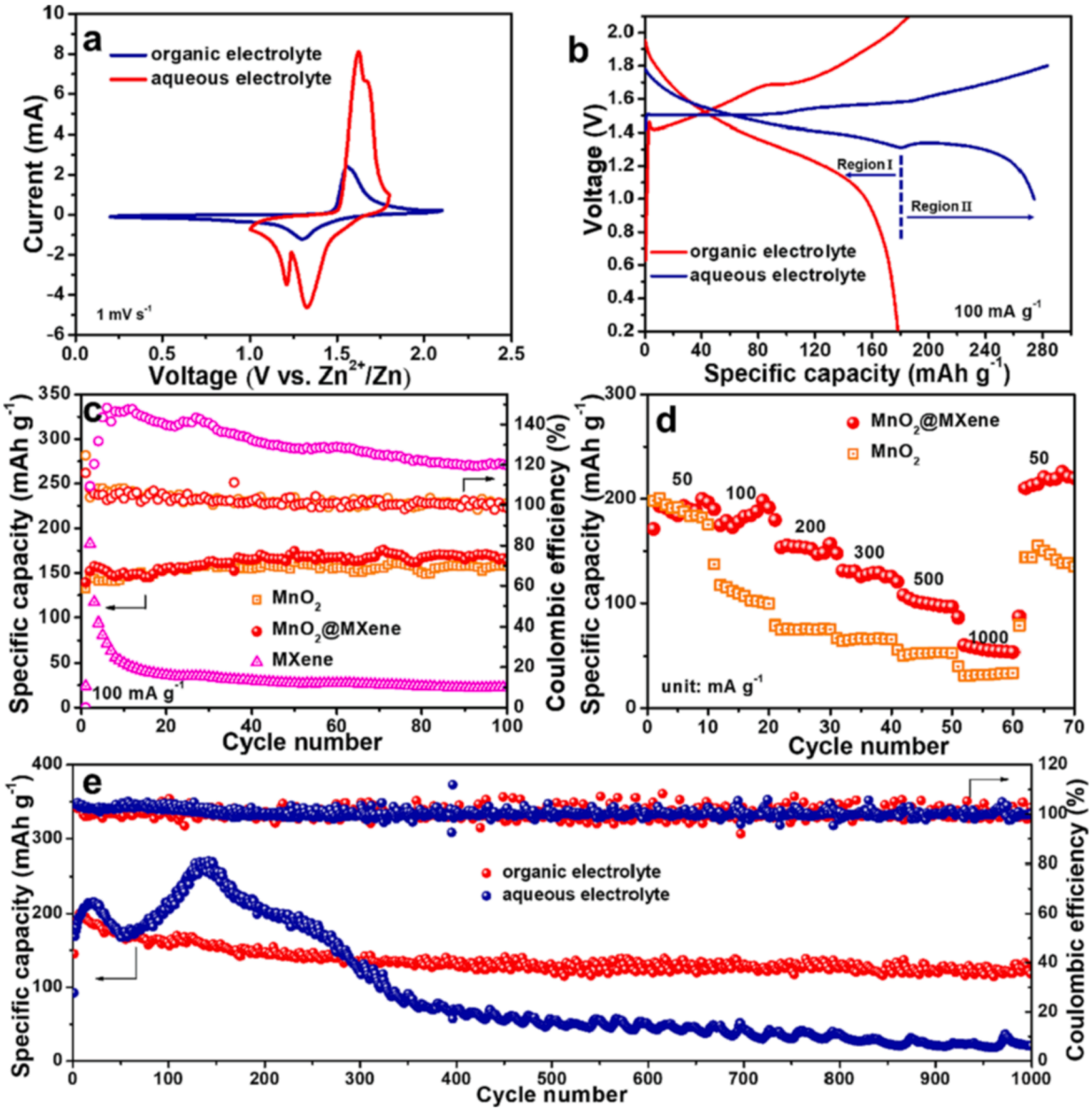

Fig. 4. Electrochemical performance of flexible MnO_2@MXene/EG films for ZIBs. (a) CV curves and (b) GCD curves of MnO_2@MXene in organic and aqueous electrolytes. (c) Cycling performance of MnO_2@MXene, MnO_2, and MXene cathodes in organic electrolyte. (d) Rate performance of MnO_2@MXene and MnO_2 cathodes in organic electrolyte. (e) Long-term cycling performance of MnO_2@MXene in organic and aqueous electrolytes.

Correspondingly, the GCD profiles also display a pair of voltage plateaus (Fig. 4b), demonstrating the unique Zn^{2+}-exclusive storage mechanism of MnO_2@MXene hybrid in $Zn(OTf)_2$/TEP electrolyte, which can effectively avoid undesired proton storage induced disadvantages and side reactions (e.g., Mn dissolution) in traditional aqueous electrolytes. To highlight the unique roles of MXene nanosheets, the cycling performance of MnO_2@MXene, MnO_2, and MXene cathodes are examined at 100 mA g^{-1}. As shown in Fig. 4c, MnO_2@MXene cathodes exhibit a specific capacity of ~163 mAh g^{-1} at 100th cycle, which obviously surpass both pure MnO_2 (157 mAh g^{-1}) and MXene cathodes (~22 mAh g^{-1}). Moreover, high capacities of 184, 178, 154, 126, 100, and 57 mAh g^{-1} are recorded at current densities of 50, 100, 200, 300, 500, and 1000 mA g^{-1}, respectively, superior to the values of MnO_2 electrode. Moreover, when the current density shifts back to 50 mA g^{-1}, a high capacity of 220.9 mAh g^{-1} can be recovered, demonstrative of fast reaction kinetics enabled by the presence of MXene (Fig. 4d). Similarly, the enhanced electrochemical performance of MnO_2@MXene thin film cathodes can be reproduced in traditional aqueous electrolyte (Figs. S8 and S9). Notably, the mass ratio of MXene in MnO_2@MXene nanosheets significantly influences the zinc storage performance, which can be easily regulated by varying the dose of MXene nanosheets during the synthesis of PDA@MXene precursor. Specifically, less MXene dose (10 mg) results in a high average capacity of 179 mAh g^{-1} at 100 mA g^{-1} but inferior rate capability (Figs. S10, S12), and more MXene dose (30 mg) leads to an undesirable average capacity of 150 mAh g^{-1} (Figs. S11, S12). The optimal zinc storage performance can be recorded in the case of MXene dose (20 mg), which corresponds to a MXene ratio of 20.7 wt% in MnO_2@MXene hybrid (Fig. S13). Further, MnO_2@MXene thin film cathode can display a high capacity retention of 84.5 % at 100 mA g^{-1} after 1000 cycles in the organic electrolyte, which is comparable to the state-of-the-art electrodes or batteries, such as Mn-metal batteries (100 % capacity retention after 200 cycles) [29], metal–organic frameworks based cathode (77.2 % capacity retention after 950 cycles) [3], and triphenylphosphine selenide organic cathode (85.3 % capacity retention after 4300 cycles) [2]. While in the case of aqueous electrolyte, an activation process is recorded during the initial 140 cycles, which is

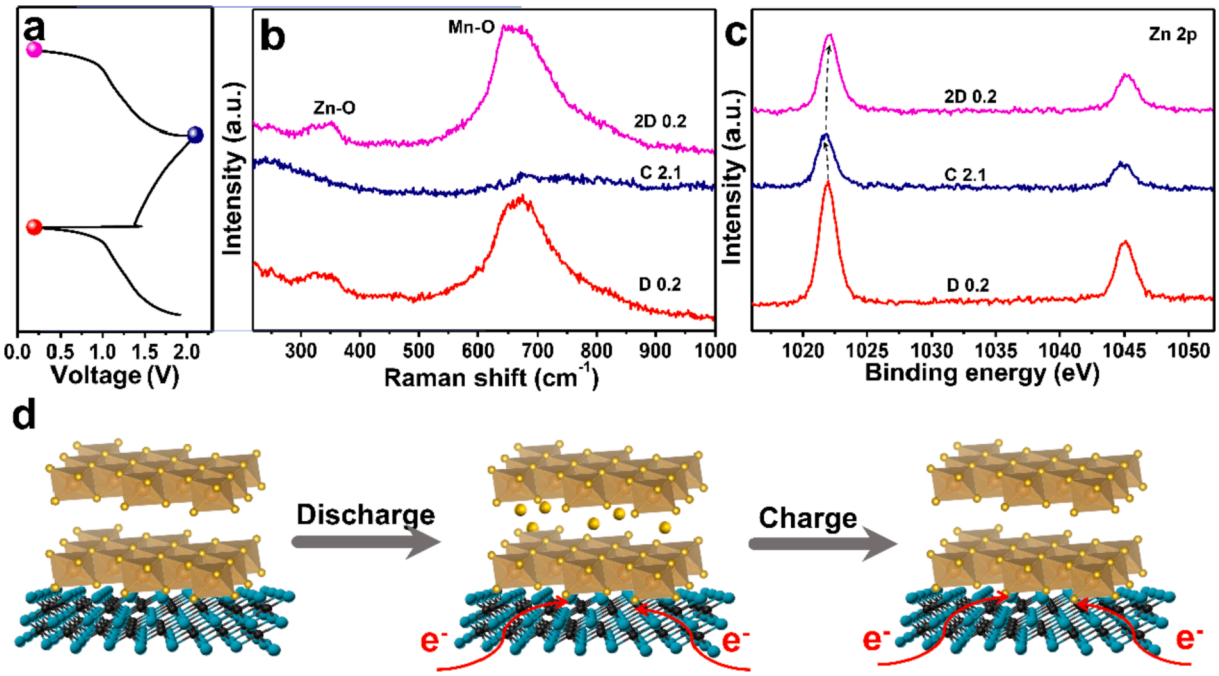

Fig. 5. Structural analysis of MnO_2@MXene cathodes at the charged (2.1 V) and discharged (0.2 V) states in organic electrolytes. (a) GCD curves. (b) Raman spectra. (c) High resolution Zn 2p XPS spectra. (d) Schematic illustration of Zn^{2+} storage mechanism in organic electrolyte.

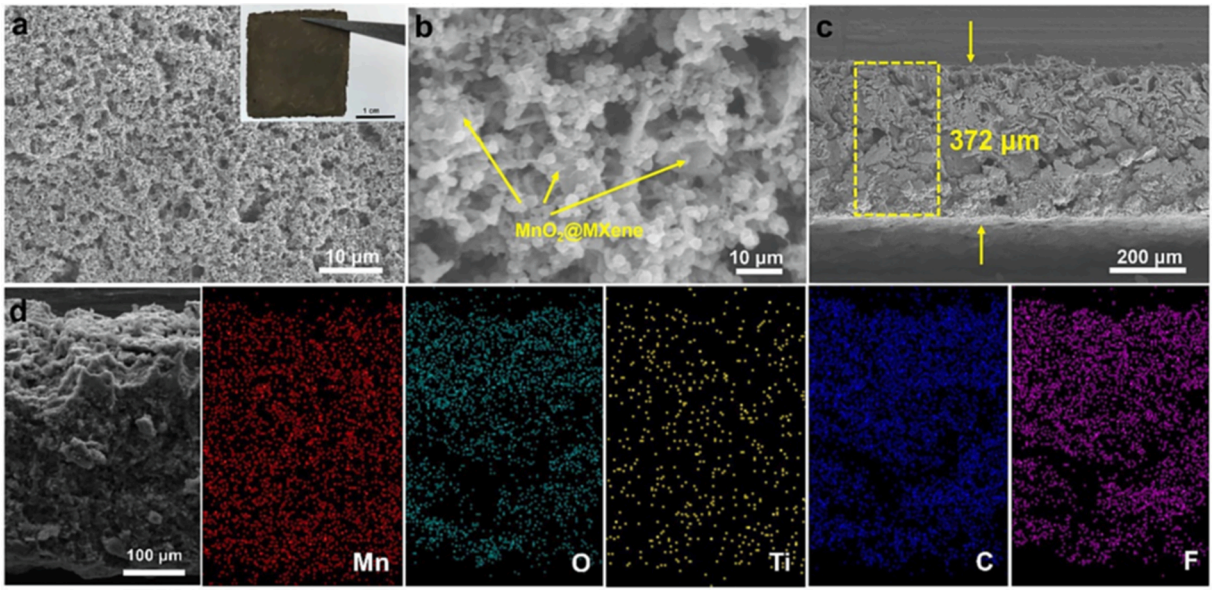

Fig. 6. Free-standing thick MnO_2@MXene films with mass loading of 10.5 mg cm^{-2} enabled by phase inversion strategy. (a, b) Optical image (inset in (a)) and top-view SEM images. (c) Cross-sectional SEM image. (d) Elemental mapping analysis on the selected zone of MnO_2@MXene films.

mainly attributed to H^+/Zn^{2+}-dominated insertion/extraction processes [37]. Subsequently, serious capacity decay in the initial 300 cycles is observed (Fig. 4e), suggestive of the superiority of the organic electrolytes over aqueous counterpart for MnO_2@MXene cathode.

To disclose the zinc storage mechanism of MnO_2@MXene cathodes in organic electrolytes, ex-situ structural characterizations were carried out to investigate the chemical composition and surface state of the electrodes in different charge/discharge states (Fig. 5a). Raman spectra recorded the structural evolution of MnO_2@MXene during charging and discharging processes (Fig. 5b). Specifically, the MnO_2@MXene cathode was firstly discharged to 0.2 V (D 0.2), and then charged to 2.1 V (C 2.1). Correspondingly, the peak at 670 cm^{-1} responding to Mn–O symmetric vibration in the [MnO_6] octahedral structure, almost disappears with negligible peak intensity. When MnO_2@MXene cathode was subsequently discharged to 0.2 V (2D 0.2) for the 2nd cycle, the peak recovers to the initial state, indicating the reversible change of interlayer spacing of MnO_2 layers. Moreover, energy dispersive X-ray spectra (EDS) spectra of MnO_2@MXene in the investigated states suggest that the peak intensity of Zn peaks are firstly reduced from D 0.2 to C 2.1 states, and meanwhile, the atomic ratio of element Mn to Zn greatly increases from 1.3 to 4.1 (Fig. S14). Notably, both the peak intensity and the atomic ratio can be recovered to the initial states at 2D 0.2 (Fig. S14). In addition, the peak of Zn 2p in the XPS spectrum of MnO_2@MXene slightly shifts to lower binding energies from D 0.2 to C 2.1 (Fig. 5c), and

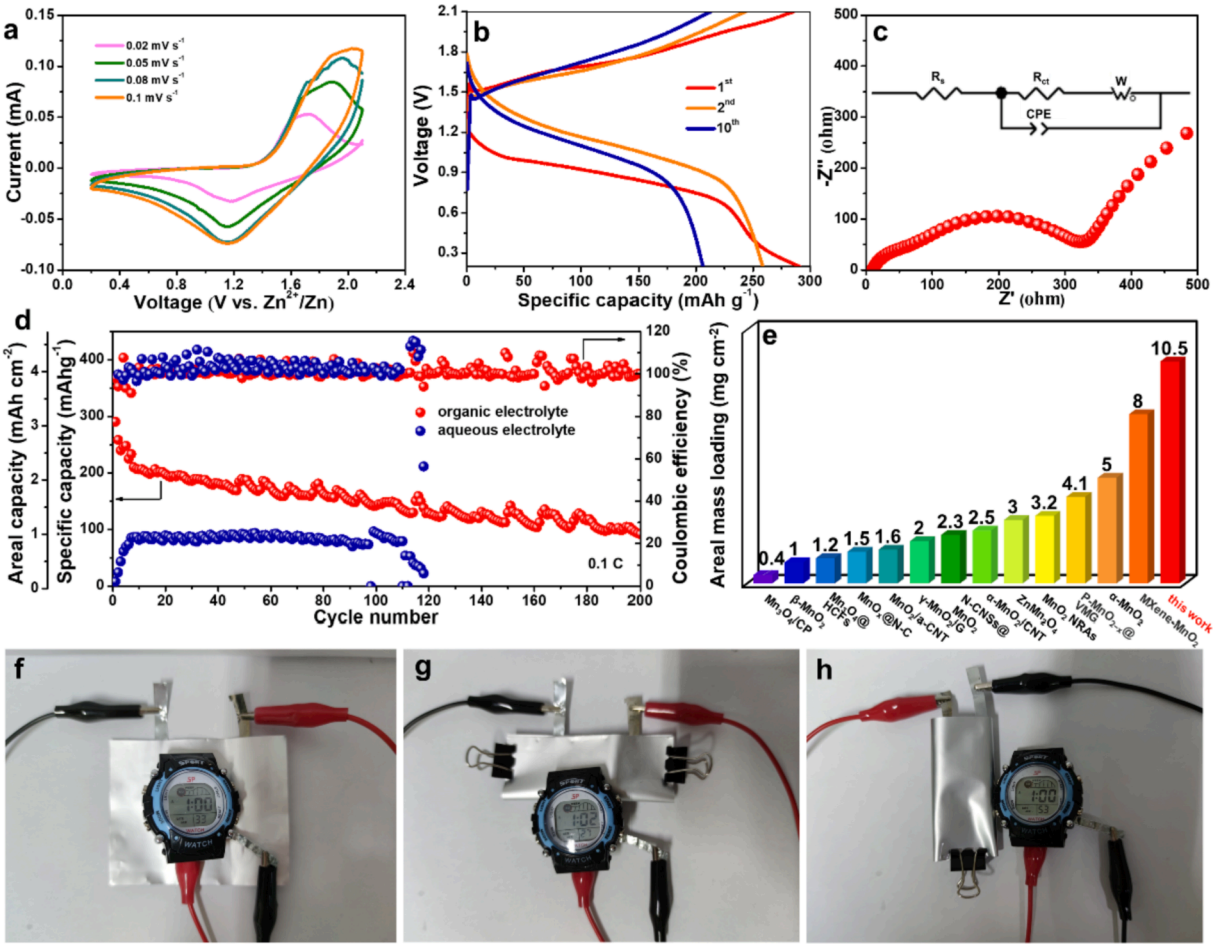

Fig. 7. Electrochemical performance of free-standing thick MnO_2@MXene films with mass loading of 10.5 mg cm^{-2} in organic electrolyte. (a) CV curves. (b) GCD profiles. (c) EIS test. (d) Cycling performance of thick MnO_2@MXene film electrodes at 0.1C in organic and aqueous electrolytes. (e) Comparison with some previously reported works on manganese based cathodes for ZIBs from the perspective of mass loading of active materials. (f–h) Three batteries connected in series could power an electronic watch under either (f) flat or (g-h) bending states.

then restores to the initial state at 2D 0.2, indicative of the reversible Zn^{2+} insertion/extraction in/from MnO_2@MXene cathodes. Based on the above results, Zn^{2+}-exclusive storage mechanism of MnO_2@MXene cathode in organic $Zn(OTf)_2$/TEP electrolyte is clearly revealed (Fig. 5d). Notably, previous works on TEP based electrolytes for ZIBs mainly focused on the issues of metal anodes, such as dendrites and side reactions [38–40]. Differently, in our work, the feasibility of TEP based electrolytes for Mn-based cathodes was demonstrated, and importantly, unique Zn^{2+}-exclusive storage mechanism without proton storage was revealed in the as-fabricated δ-MnO_2/MXene cathodes.

The excellent zinc storage performance of MnO_2@MXene heteronanosheets encourages us to further construct thick film electrode with a high mass loading up to 10.5 mg cm^{-2} (Fig. 6a). SEM image of the free-standing MnO_2@MXene thick film demonstrates the presence of abundant macropores and MnO_2@MXene heteronanosheets and auxiliary materials (carbon black and PVDF) (Fig. 6a-b). Notably, the thickness of the film can be up to 372 μm (Fig. 6c), and importantly, the thickness could be precisely controlled in a large range (e.g., 128, 268, and 372 μm) (Fig. S15) corresponding to the mass loading ranging from 2.1 to 10.5 mg cm^{-2}. Furthermore, XRD patterns were employed to confirm the main component of MnO_2@MXene nanosheets, in which the characteristic peaks of δ-MnO_2 appear at ~25.4°, ~37.7° and ~65.5° (Fig. S16). Moreover, elemental mapping analysis further reveals the uniform distribution of Mn, O, C, Ti, and F elements in the investigated area of the free-standing thick film (Fig. 6d).

The zinc storage performance of MnO_2@MXene based thick film cathodes in the developed organic electrolyte was systematically investigated. As shown in Fig. 7a, a pair of cathodic and anodic peaks can be observed at 1.18 and 1.71 V in the CV curves of the MnO_2@MXene based thick film electrode at 0.02 mV s^{-1}. Correspondingly, one-step Zn^{2+} insertion/extraction in/out of layered MnO_2 reflect in the GCD profiles (Fig. 7b). EIS measurement further indicates a charge transfer resistance (R_{ct}) of 358.6 Ω (Fig. 7c). Notably, MnO_2@MXene thick film cathode delivers a capacity of 290 mAh g^{-1} (3.05 mAh cm^{-2}) and 142 mAh g^{-1} (1.49 mAh cm^{-2}) for the 1st and 100th cycles at 0.1C (1C = 308 mAh g^{-1}) in organic $Zn(OTf)_2$/TEP electrolyte (Fig. 7d), respectively. While in the case of aqueous electrolyte, the thick film electrode only displays low capacities (<100 mAh g^{-1}) in the initial 100 cycles, and the cell fails after 120 cycles. Notably, such high areal mass loading of 10.5 mg cm^{-2} of this thick film electrode surpasses those of the most reported ZIBs with manganese-based cathodes (Fig. 7e), such as electrodeposited Mn_3O_4 on carbon paper (Mn_3O_4/CP, 0.4 mg cm^{-2}) [41], nanorod β-MnO_2 (1 mg cm^{-2}) [42], Mn_3O_4 nanoparticles encapsulated in the hollow carbon fibers (Mn_3O_4@HCFs, 1.2 mg cm^{-2}) [43], onion-like *N*-doped carbon nanowalls coated MnO_x nanorods (MnO_x@N—C, 1.5 mg cm^{-2}) [44], MnO_2 nanorods on acid-treated carbon nanotube (MnO_2/a-CNT, 1.6 mg cm^{-2}) [45], γ-MnO_2-graphene composite (γ-MnO_2/G, 2 mg cm^{-2}) [46], MnO_2 anchored on nitrogen-doped porous carbon nanosheets (*N*-CNSs@MnO_2, 2.3 mg cm^{-2}) [14], α-MnO_2 nanofibers/CNT hierarchically assembled microspheres (α-MnO_2/CNT, 2.5 mg cm^{-2}) [47], $ZnMn_2O_4$ (3 mg cm^{-2}) [48], MnO_2 nanorod arrays (MnO_2 NRAs, 3.2 mg cm^{-2}) [49], phosphate ions

intercalated manganese dioxide/vertical multilayer graphene (VMG) arrays with oxygen defects (P-MnO_{2-x}@VMG, 4.1 mg cm^{-2}) [50], α-MnO_2 (5 mg cm^{-2}) [22], and MXene-MnO_2 microflowers (8 mg cm^{-2}) [20]. Besides, three MnO_2@MXene based Zn-MnO_2 batteries connected in series can readily power an electronic watch under either normal or bending states (Fig. 7f-h), demonstrative of the promising applications of our organic Zn-MnO_2 batteries in flexible devices.

4. Conclusions

In summary, we successfully developed an interfacial assembly strategy to prepare strongly-coupled MnO_2@MXene heteronanosheets via an in-situ polymerization of dopamine on Ti_3C_2 MXene nanosheets and subsequent redox reaction between $KMnO_4$ and polydopamine, in which thin layered δ-MnO_2 nanoflakes vertically deposited on conductive MXene nanosheets greatly facilitated fast electron/ion transfer kinetics and structural stability. Importantly, the MnO_2@MXene heteronanosheets exhibited a unique Zn^{2+}-exclusive storage mechanism in our developed organic electrolyte of $Zn(OTf)_2$/TEP, avoiding undesired proton storage induced disadvantages and side reactions (e.g., Mn dissolution) in traditional aqueous electrolyte. Therefore, the MnO_2@MXene heteronanosheet based film cathode exhibited prominent zinc storage performance, such as a high capacity retention of 84.5 % for 1000 cycles and a high areal capacity of 1.9 mAh cm^{-2} at a mass loading of 10.5 mg cm^{-2}. This work will pave a new way to construct high-performance ZIBs via the rational design of manganese-based cathodes and selection of suitable electrolytes with unique Zn^{2+}-exclusive storage mechanisms.

Declaration of Competing Interest

The authors declare that they have no known competing financial interests or personal relationships that could have appeared to influence the work reported in this paper.

Data availability

Data will be made available on request.

Acknowledgments

This work was financially supported by the National Natural Science Foundation of China (Grant. 22125903), the Liao Ning Revitalization Talents Program (XLYC2007129), Dalian National Laboratory For Clean Energy (DNL), CAS, DNL Cooperation Fund, CAS (DNL202016, DNL202019), DICP (DICP I2020032), the Joint Fund of the Yulin University and the Dalian National Laboratory for Clean Energy (YLU-DNL Fund 2021002, YLU-DNL Fund 2021009), the Fundamental Research Funds for the Central Universities of China (N2105008), and the fund of the State Key Laboratory of Catalysis in DICP (N-21-03).

Appendix A. Supplementary data

Supplementary data to this article can be found online at https://doi.org/10.1016/j.cej.2023.141662.

References

[1] D. Chao, W. Zhou, F. Xie, C. Ye, H. Li, M. Jaroniec, S.-Z. Qiao, Roadmap for advanced aqueous batteries: from design of materials to applications, Sci. Adv. 6 (2020) eaba4098.
[2] Z. Chen, H. Cui, Y. Hou, X. Wang, X. Jin, A. Chen, Q. Yang, D. Wang, Z. Huang, C. Zhi, Anion chemistry enabled positive valence conversion to achieve a record high-voltage organic cathode for zinc batteries, Chem 8 (2022) 1–13.
[3] S. Yang, H. Lv, Y. Wang, X. Guo, L. Zhao, H. Li, C. Zhi, Regulating exposed facets of metal-organic frameworks for high-rate alkaline aqueous zinc batteries, Angew. Chem. Int. Ed. 61 (2022) e202209794.
[4] Z. Pei, Symmetric is nonidentical: operation history matters for Zn metal anode, Nano Res. Energy 1 (2022) e9120023.
[5] C. Xu, B. Li, H. Du, F. Kang, Energetic zinc ion chemistry: the rechargeable zinc ion battery, Angew. Chem. Int. Ed. 51 (4) (2012) 933–935.
[6] Y. Zhao, Y. Zhu, X. Zhang, Challenges and perspectives for manganese-based oxides for advanced aqueous zinc-ion batteries, InfoMat 2 (2) (2020) 237–260.
[7] M. Huang, F. Li, F. Dong, Y.X. Zhang, L.L. Zhang, MnO_2-based nanostructures for high-performance supercapacitors, J. Mater. Chem. A 3 (43) (2015) 21380–21423.
[8] B. Lee, C.S. Yoon, H.R. Lee, K.Y. Chung, B.W. Cho, S.H. Oh, Electrochemically-induced reversible transition from the tunneled to layered polymorphs of manganese dioxide, Sci. Rep. 4 (2014) 6066.
[9] H. Ge, X. Feng, D. Liu, Y. Zhang, Recent advances and perspectives for Zn-based batteries: Zn anode and electrolyte, Nano Res. Energy 2 (2023) e9120039.
[10] L. Wu, Y. Dong, Recent progress of carbon nanomaterials for high-performance cathodes and anodes in aqueous zinc ion batteries, Energy Storage Mater. 41 (2021) 715–737.
[11] X. Yuan, F. Ma, L. Zuo, J. Wang, N. Yu, Y. Chen, Y. Zhu, Q. Huang, R. Holze, Y. Wu, T. van Ree, Latest advances in high-voltage and high-energy-density aqueous rechargeable batteries, Electrochem. Energy Rev. 4 (1) (2021) 1–34.
[12] J. Huang, Z. Wang, M. Hou, X. Dong, Y. Liu, Y. Wang, Y. Xia, Polyaniline-intercalated manganese dioxide nanolayers as a high-performance cathode material for an aqueous zinc-ion battery, Nat. Commun. 9 (2018) 2906.
[13] W. Yang, L. Dong, W. Yang, C. Xu, G. Shao, G. Wang, 3D oxygen-defective potassium vanadate/carbon nanoribbon networks as high-performance cathodes for aqueous zinc-ion batteries, Small Methods 4 (2020) 1900670.
[14] Y. Zhang, S. Deng, Y. Li, B. Liu, G. Pan, Q. Liu, X. Wang, X. Xia, J. Tu, Anchoring MnO_2 on nitrogen-doped porous carbon nanosheets as flexible arrays cathodes for advanced rechargeable Zn-MnO_2 batteries, Energy Storage Mater. 29 (2020) 52–59.
[15] M. Song, H. Tan, D. Chao, H. Fan, Recent advances in Zn-ion batteries, Adv. Funct. Mater. 28 (2018) 1802564.
[16] L. Wu, M. Zhang, W. Xu, Y. Dong, Recent advances in carbon materials for flexible zinc ion batteries, New Carbon Mater. 37 (5) (2022) 827–851.
[17] Y. Dong, H. Shi, Z.-S. Wu, Recent advances and promise of MXene-based nanostructures for high-performance metal ion batteries, Adv. Funct. Mater. 30 (2020) 2000706.
[18] Y. Gogotsi, Q. Huang, MXenes: two-dimensional building blocks for future materials and devices, ACS Nano 15 (2021) 5775–5780.
[19] G. Liang, X. Li, Y. Wang, S. Yang, Z. Huang, Q. Yang, D. Wang, B. Dong, M. Zhu, C. Zhi, Building durable aqueous K-ion capacitors based on MXene family, Nano Res. Energy 1 (2022) e9120002.
[20] M. Shi, B. Wang, C. Chen, J. Lang, C. Yan, X. Yan, 3D high-density MXene@MnO_2 microflowers for advanced aqueous zinc-ion batteries, J. Mater. Chem. A 8 (46) (2020) 24635–24644.
[21] X. Zhu, Z. Cao, W. Wang, H. Li, J. Dong, S. Gao, D. Xu, L. Li, J. Shen, M. Ye, Superior-performance aqueous zinc-ion batteries based on the in situ growth of MnO_2 nanosheets on V_2CT_X MXene, ACS Nano 15 (2) (2021) 2971–2983.
[22] H. Pan, Y. Shao, P. Yan, Y. Cheng, K.S. Han, Z. Nie, C. Wang, J. Yang, X. Li, P. Bhattacharya, K.T. Mueller, J. Liu, Reversible aqueous zinc/manganese oxide energy storage from conversion reactions, Nat. Energy 1 (2016) 1–7.
[23] X. Shen, X. Wang, Y. Zhou, Y. Shi, L. Zhao, H. Jin, J. Di, Q. Li, Highly reversible aqueous Zn-MnO_2 battery by supplementing Mn^{2+}-mediated MnO_2 deposition and dissolution, Adv. Funct. Mater. 31 (2021) 2101579.
[24] C.F. Bischoff, O.S. Fitz, J. Burns, M. Bauer, H. Gentischer, K.P. Birke, H.-M. Henning, D. Biro, Revealing the local pH value changes of acidic aqueous zinc ion batteries with a manganese dioxide electrode during cycling, J. Electrochem. Soc. 167 (2020), 020545.
[25] X. Yang, H. Zhang, Y. Chen, Y. Yu, X. Li, H. Zhang, Shapeable electrodes with extensive materials options and ultra-high loadings for energy storage devices, Nano Energy 39 (2017) 418–428.
[26] X. Yang, Y. Chen, M. Wang, H. Zhang, X. Li, H. Zhang, Phase inversion: a universal method to create high-performance porous electrodes for nanoparticle-based energy storage devices, Adv. Funct. Mater. 26 (2016) 8427–8434.
[27] P. Shang, Y. Liu, Y. Mei, L. Wu, Y. Dong, Defective MnO_2 nanosheets based free-standing and high mass loading electrodes for high energy density aqueous zinc ion batteries, Mater. Chem. Front. 5 (22) (2021) 8002–8009.
[28] X. Liu, W. Wei, Y. Yang, Y. Li, Y. Li, S. Xu, Y. Dong, R. He, A porous membrane electrolyte enabled by poly(biphenyl piperidinium triphenylmethane) for dendrite-free zinc anode with enhanced cycling life, Chem. Eng. J. 437 (2022), 135409.
[29] Q. Yang, X. Qu, H. Cui, X. He, Y. Shao, Y. Zhang, X. Guo, A. Chen, Z. Chen, R. Zhang, Rechargeable aqueous Mn-metal battery enabled by inorgani-organic interfaces, Angew. Chem. Int. Ed. 61 (2022) e202206471.
[30] H. Liu, B. Wang, M. Chen, H. Zhang, J. Peng, L. Ding, W. Wang, Simple synthesis of BiOAc/BiOBr heterojunction composites for the efficient photocatalytic removal of organic pollutants, Sep. Purif. Technol. 261 (2021), 118286.
[31] M.C. Basso, A. Pizzi, J.P. Maris, L. Delmotte, B. Colin, Y. Rogaume, MALDI-TOF, 13C NMR and FTIR analysis of the cross-linking reaction of condensed tannins by triethyl phosphate, Ind. Crop. Prod. 95 (2017) 621–631.
[32] Y. Mei, Y. Liu, W. Xu, M. Zhang, Y. Dong, J. Qiu, Suppressing vanadium dissolution in 2D V_2O_5/MXene heterostructures via organic/aqueous hybrid electrolyte for stable zinc ion batteries, Chem. Eng. J. 452 (2023), 139574.
[33] X. Qiu, N. Wang, X. Dong, J. Xu, K. Zhou, W. Li, Y. Wang, A high-voltage Zn-organic battery using a nonflammable organic electrolyte, Angew. Chem. Int. Ed. 60 (38) (2021) 21025–21032.

[34] D. Kundu, S. Hosseini Vajargah, L. Wan, B. Adams, D. Prendergast, L.F. Nazar, Aqueous vs. nonaqueous Zn-ion batteries: consequences of the desolvation penalty at the interface, Energy Environ. Sci. 11 (2018) 881–892.
[35] H. Luo, B. Liu, Z. Yang, Y. Wan, C. Zhong, The trade-offs in the design of reversible zinc anodes for secondary alkaline batteries, Electrochem. Energy Rev. 5 (1) (2022) 187–210.
[36] F. Shi, C. Mang, H. Liu, Y. Dong, Flexible and high-energy-density Zn/MnO_2 batteries enabled by electrochemically exfoliated graphene nanosheets, New J. Chem. 44 (3) (2020) 653–657.
[37] H. Yang, W. Zhou, D. Chen, J. Liu, Z. Yuan, M. Lu, L. Shen, V. Shulga, W. Han, D. Chao, The origin of capacity fluctuation and rescue of dead Mn-based Zn–ion batteries: a Mn-based competitive capacity evolution protocol, Energy Environ. Sci. 15 (2022) 1106–1118.
[38] L. Xiao, Z. Zeng, X. Liu, Y. Fang, X. Jiang, Y. Shao, L. Zhuang, X. Ai, H. Yang, Y. Cao, J. Liu, Stable Li metal anode with "ion–solvent-coordinated" nonflammable electrolyte for safe Li metal batteries, ACS Energy Lett. 4 (2) (2019) 483–488.
[39] H. Zhang, J. Luo, M. Qi, S. Lin, Q. Dong, H. Li, N. Dulock, C. Povinelli, N. Wong, W. Fan, J. Bao, D. Wang, Enabling lithium metal anode in nonflammable phosphate electrolyte with electrochemically induced chemical reactions, Angew. Chem. Int. Ed. 60 (35) (2021) 19183–19190.
[40] H. Yang, Q. Li, C. Guo, A. Naveed, J. Yang, Y. Nuli, J. Wang, Safer lithium-sulfur battery based on nonflammable electrolyte with sulfur composite cathode, Chem. Commun. 54 (33) (2018) 4132–4135.
[41] A. Dhiman, D.G. Ivey, Electrodeposited manganese oxide on carbon paper for zinc-ion battery cathodes, Batteries Supercaps 3 (3) (2020) 293–305.
[42] W. Liu, X. Zhang, Y. Huang, B. Jiang, Z. Chang, C. Xu, F. Kang, β-MnO_2 with proton conversion mechanism in rechargeable zinc ion battery, J. Energy Chem. 56 (2021) 365–373.
[43] J. Long, Z. Yang, F. Yang, J. Cuan, J. Wu, Electrospun core-shell Mn_3O_4/carbon fibers as high-performance cathode materials for aqueous zinc-ion batteries, Electrochim. Acta 344 (2020), 136155.
[44] Y. Fu, Q. Wei, G. Zhang, X. Wang, J. Zhang, Y. Hu, D. Wang, L. Zuin, T. Zhou, Y. Wu, S. Sun, High-performance reversible aqueous Zn-ion battery based on porous MnO_x nanorods coated by MOF-derived N-doped carbon, Adv. Energy Mater. 8 (26) (2018) 1801445.
[45] D. Xu, B. Li, C. Wei, Y.-B. He, H. Du, X. Chu, X. Qin, Q.-H. Yang, F. Kang, Preparation and characterization of MnO_2/acid-treated CNT nanocomposites for energy storage with zinc ions, Electrochim. Acta 133 (2014) 254–261.
[46] C. Wang, Y. Zeng, X. Xiao, S. Wu, G. Zhong, K. Xu, Z. Wei, W. Su, X. Lu, γ-MnO_2 nanorods/graphene composite as efficient cathode for advanced rechargeable aqueous zinc-ion battery, J. Energy Chem. 43 (2020) 182–187.
[47] Y. Liu, X. Chi, Q. Han, Y. Du, J. Huang, Y. Liu, J. Yang, α-MnO_2 nanofibers/carbon nanotubes hierarchically assembled microspheres: approaching practical applications of high-performance aqueous Zn-ion batteries, J. Power Sources 443 (2019) 227244.
[48] X. Wu, Y. Xiang, Q. Peng, X. Wu, Y. Li, F. Tang, R. Song, Z. Liu, Z. He, X. Wu, Green-low-cost rechargeable aqueous zinc-ion batteries using hollow porous spinel $ZnMn_2O_4$ as the cathode material, J. Mater. Chem. A 5 (34) (2017) 17990–17997.
[49] W. Qiu, Y. Li, A. You, Z. Zhang, G. Li, X. Lu, Y. Tong, High-performance flexible quasi-solid-state Zn-MnO_2 battery based on MnO_2 nanorod arrays coated 3D porous nitrogen-doped carbon cloth, J. Mater. Chem. A 5 (28) (2017) 14838–14846.
[50] Y. Zhang, S. Deng, G. Pan, H. Zhang, B. Liu, X.L. Wang, X. Zheng, Q. Liu, X. Wang, X. Xia, J. Tu, Introducing oxygen defects into phosphate ions intercalated manganese dioxide/vertical multilayer graphene arrays to boost flexible zinc ion storage, Small Methods 4 (2020) 1900828.